Structural Engineering and Mechanics, Vol. 40, No. 3 (2011) 393-410
DOI: http://dx.doi.org/10.12989/sem.2011.40.3.393

An incompatible 3D solid element for structural analysis at elevated temperatures

Xinmeng Yu*[1], Xiaoxiong Zha[1] and Zhaohui Huang[2]

[1]*Department of Civil and Environmental Engineering, Shenzhen Graduate School of Harbin Institute of Technology, Shenzhen 518055, China*
[2]*Department of Civil and Structural Engineering, University of Sheffield, Sheffield S1 3JD, UK*

(Received January 14, 2011, Revised July 17, 2011, Accepted August 17, 2011)

Abstract. The eight-node 3D solid element is one of the most extensively used elements in computational mechanics. This is due to its simple shape and easy of discretization. However, due to the parasitic shear locking, it should not be used to simulate the behaviour of structural members in bending dominant conditions. Previous researches have indicated that the introduction of incompatible mode into the displacement field of the solid element could significantly reduce the shear locking phenomenon. In this study, an incompatible mode eight-node solid element, which considers both geometric and material nonlinearities, is developed for modelling of structural members at elevated temperatures. An algorithm is developed to extend the state determination procedure at ambient temperature to elevated temperatures overcoming initially converged stress locking when the external load is kept constant. Numerical studies show that this incompatible element is superior in terms of convergence, mesh insensitivity and reducing shear locking. It is also showed that the solid element model developed in this paper can be used to model structural behaviour at both ambient and elevated temperatures.

Keywords: incompatible mode; solid 3D element; shear locking; elevated temperature; initially converged stress locking

1. Introduction

One of the most important weakness of any structural system - in particular, steel structures -is the dramatic reduction of its mechanical resistance as soon as they are exposed to the action of fire, due to the rapid degradation of their material properties associated to the development of high gradients of temperature. The typical numerical analysis of this kind of scenarios does not take care of these conditions, and it could be relevant if it is necessary to evaluate the real response of the structure. By the way, in these numerical simulations the structural members subjected to bending loads are usually analyzed by beam/column elements. It is generally believed that finite beam/column assembly can achieve reasonable accuracy with relative low computing cost in modelling the global behaviour of the structural members. The shortcoming of this family of elements lies in the difficultness in simulating perforated members, laterally confined members, or irregular members experiencing stress intensity, e.g., localized failure. In these circumstances, solid elements are

*Corresponding author, Ph.D., E-mail: xinmengyu@gmail.com

preferable, especially when stress distribution in the structural members is a major concern. In addition, in order to reduce computing cost in structural analysis, a better choice is to use low order elements such as 8-node linearly interpolated solid elements. Combined with other types of elements, an enhanced solid element can be developed for modelling of reinforced concrete structures (Dominguez *et al.* 2010). Solid-like shell elements can also be obtained from the solid element model with some modifications (Abed-Meraim and Combescure 2011).

In the classical finite element method (FEM) theories the displacement compatibility between finite elements is absolutely mandatory. However, it has been well known that the displacement compatible four-node quadrilateral and eight-node hexahedral elements suffer from severe shear locking when they are subjected to bending. This parasitic drawback of the elements can produce significant errors when these elements are used in practical engineering analysis. A remedy to eliminate shear locking of the elements is to reduce the stiffness in the integration process. Reduced or selective integration scheme has a softening effect due to some polynomial terms vanish at Gauss points with a low-order rule and therefore make no contribution to the strain energy. But this under-integration approach introduces the defects variously known as spurious mode, instability and mechanism. A disadvantage of the selective integration scheme is that the shear strain is not frame-invariant, which is guaranteed by consistent use of the same shape functions for all components of displacement (Cook *et al.* 2002). Another disadvantage of the selective integration is that the shear stresses are evaluated at positions different from those in the full integration scheme. This is a big problem when material nonlinearity is involved. The first introduction of the incompatible displacements into rectangular isoparametric finite elements by Wilson *et al.* (1971) showed the superior capability in eliminating shear locking and improving numerical convergence. The principle of the incompatible mode is to enhance linear elements with extra degrees of freedom which count for internal parabolic deformation in bending, without affecting node positions. This incompatible mode attracted so much research attention that patch test theories were developed to overcome the compatible restriction (Irons and Razzaque 1972, Taylor *et al.* 1986). Lots of works have been done to achieve high accuracy low-order incompatible elements such as B-bar method (Hughes 1980) and assumed strain method (Simo and Rafai 1974). A least-squares stress recovery method (Ibrahimbegovic and Wilson 1991) was introduced to improve the accuracy of stress computation.

In this research, the displacement incompatible 8-node solid element (*SOLID8IC*, and hereafter) is developed to perform nonlinear stress analyses in structures at elevated temperatures. In this element, a unified three dimensional isotropic yielding model (Owen and Hinton 1980) is applied and an algorithm, which considers material degradation at elevated temperatures, is developed to extend the material state determination procedure at ambient temperature to elevated temperatures without being locked by the initially converged stresses attained.

2. The finite element procedure of SOLID8IC

The eight-node solid element exhibits shear locking, thus to be excessively stiff due to spurious shear strain in bending. The basic idea of eliminating shear locking is to add bending modes to the displacement fields of the classical 8-node hexahedral element. This can be done by appending arbitrary selected displacement interpolation functions to the classical interpolations as shown in Eq. (1).

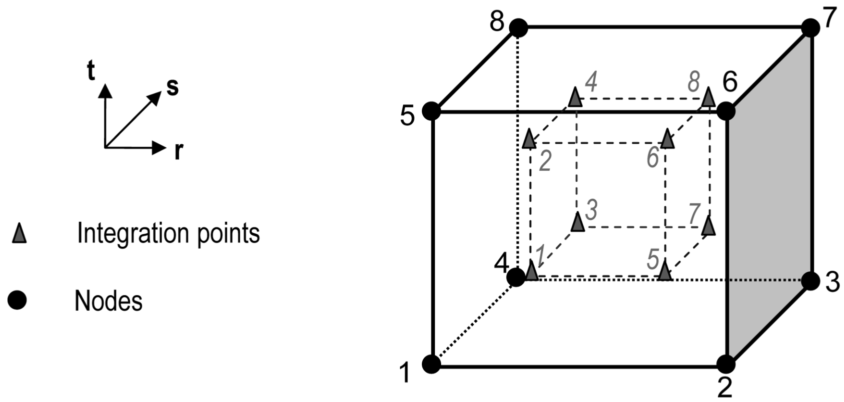

Fig. 1 The master cube of the eight-node solid element and its integration points

$$\begin{cases} u = \sum_{i=1}^{8} N_i u_i + \sum_{i=9}^{11} N_i \alpha_i^u \\ v = \sum_{i=1}^{8} N_i v_i + \sum_{i=9}^{11} N_i \alpha_i^v \\ w = \sum_{i=1}^{8} N_i w_i + \sum_{i=9}^{11} N_i \alpha_i^w \end{cases} \tag{1}$$

where: u, v and w are the translational displacements related to the global coordinates, x, y and z, respectively and α_i^u, α_i^v and α_i^w are extra degrees of freedom (DoF, and hereafter) representing the magnitude of incompatible modes. The N_1 to N_8 are classical nodal shape functions and the N_9 to N_{11} are shape functions correspond to the incompatible modes enhancement. The complete shape functions in local coordinate system, r-s-t, are given in Eq. (2), while the positions of the integration points ($2 \times 2 \times 2$) is shown in Fig. 1.

$$\begin{cases} N_1 = \frac{1}{8}(1-r)(1-s)(1-t) & N_5 = \frac{1}{8}(1-r)(1-s)(1+t) \\ N_2 = \frac{1}{8}(1+r)(1-s)(1-t) & N_6 = \frac{1}{8}(1+r)(1-s)(1+t) \\ N_3 = \frac{1}{8}(1+r)(1+s)(1-t) & N_7 = \frac{1}{8}(1+r)(1+s)(1+t) \\ N_4 = \frac{1}{8}(1-r)(1+s)(1-t) & N_8 = \frac{1}{8}(1-r)(1+s)(1+t) \end{cases} \tag{2a}$$

$$\begin{cases} N_9 = 1 - r^2 \\ N_{10} = 1 - s^2 \\ N_{11} = 1 - t^2 \end{cases} \tag{2b}$$

2.1 Strain-displacement relationship

From Eq. (1), the enhanced strain-displacement relationship can be written as

$$\boldsymbol{\varepsilon} = [\mathbf{B}_C \ \ \mathbf{B}_I]\begin{Bmatrix} \mathbf{u} \\ \boldsymbol{\alpha} \end{Bmatrix} - \boldsymbol{\varepsilon}_0 \tag{3}$$

where

$$\boldsymbol{\varepsilon} = \{\varepsilon_x \ \ \varepsilon_y \ \ \varepsilon_z \ \ \gamma_{xy} \ \ \gamma_{yz} \ \ \gamma_{zx}\}^T \tag{4a}$$

where $\varepsilon_x, \varepsilon_y$ and ε_z are axial strains, and γ_{xy}, γ_{yz} and γ_{zx} are shear strains; and

$$\boldsymbol{\varepsilon}_0 = \boldsymbol{\varepsilon}_T + \boldsymbol{\varepsilon}^p \tag{4b}$$

where $\boldsymbol{\varepsilon}_T$ and $\boldsymbol{\varepsilon}^p$ are thermal strains and permanent (plastic) strains, respectively

$$\mathbf{u} = \{u_1 \ \ v_1 \ \ w_1 \ \ \dots \ \ u_8 \ \ v_8 \ \ w_8\}^T \tag{4c}$$

$$\boldsymbol{\alpha} = \{\alpha_1^u \ \ \alpha_2^u \ \ \alpha_3^u \ \ \alpha_1^v \ \ \alpha_2^v \ \ \alpha_3^v \ \ \alpha_1^w \ \ \alpha_2^w \ \ \alpha_3^w\}^T \tag{4d}$$

The slightly different orders of the terms in $\boldsymbol{\alpha}$ and $\mathbf{u}$ ensure the compatible $\mathbf{B}_C$ and the incompatible $\mathbf{B}_I$ have a similar form. It can be easily derived that $\mathbf{B}_I$ is

$$\mathbf{B}_I = \begin{bmatrix} \frac{\partial N_9}{\partial x} & 0 & 0 & \cdots & \frac{\partial N_{11}}{\partial x} & 0 & 0 \\ 0 & \frac{\partial N_9}{\partial y} & 0 & \cdots & 0 & \frac{\partial N_{11}}{\partial y} & 0 \\ 0 & 0 & \frac{\partial N_9}{\partial z} & \cdots & 0 & 0 & \frac{\partial N_{11}}{\partial z} \\ \frac{\partial N_9}{\partial y} & \frac{\partial N_9}{\partial x} & 0 & \cdots & \frac{\partial N_{11}}{\partial y} & \frac{\partial N_{11}}{\partial x} & 0 \\ 0 & \frac{\partial N_9}{\partial z} & \frac{\partial N_9}{\partial y} & \cdots & 0 & \frac{\partial N_{11}}{\partial z} & \frac{\partial N_{11}}{\partial y} \\ \frac{\partial N_9}{\partial z} & 0 & \frac{\partial N_9}{\partial x} & \cdots & \frac{\partial N_{11}}{\partial z} & 0 & \frac{\partial N_{11}}{\partial x} \end{bmatrix} \tag{5}$$

For total Lagrangian description of large displacements, when incremental algorithm is used, the $\mathbf{B}_C$ is composed of small-linear displacement related $\mathbf{B}_{L1}$ and linearized initial displacement effect related $\mathbf{B}_{L2}$ (Bathe 1996). Therefore

$$\mathbf{B}_C = \mathbf{B}_{L1} + \mathbf{B}_{L2} \tag{6}$$

where $\mathbf{B}_{L1}$ is a 6 by 24 matrix with a similar form as $\mathbf{B}_I$, and

$$\mathbf{B}_{L2} = \begin{bmatrix} \cdots & l_{11}N_{i,1} & l_{21}N_{i,1} & l_{31}N_{i,1} & \cdots \\ \cdots & l_{12}N_{i,2} & l_{22}N_{i,2} & l_{32}N_{i,2} & \cdots \\ \cdots & l_{13}N_{i,3} & l_{23}N_{i,3} & l_{33}N_{i,3} & \cdots \\ \cdots & l_{11}N_{i,2}+l_{12}N_{i,1} & l_{21}N_{i,2}+l_{22}N_{i,1} & l_{31}N_{i,2}+l_{32}N_{i,1} & \cdots \\ \cdots & l_{12}N_{i,3}+l_{13}N_{i,2} & l_{22}N_{i,3}+l_{23}N_{i,2} & l_{32}N_{i,3}+l_{33}N_{i,2} & \cdots \\ \cdots & l_{11}N_{i,3}+l_{13}N_{i,1} & l_{21}N_{i,3}+l_{23}N_{i,1} & l_{31}N_{i,3}+l_{33}N_{i,1} & \cdots \end{bmatrix} \tag{7}$$

where $l_{ij} = \partial u_i/\partial x_j$ and $N_{i,j} = \partial N_i/\partial x_j$, with $x_1 \equiv x, x_2 \equiv y, x_3 \equiv z$ and $u_1 \equiv u, u_2 \equiv v, u_3 \equiv w$. x, y and z are undeformed configuration coordinates.

2.2 Correction matrix

A general approach to ensure the incompatible mode to pass the patch test is to make the strain energy associated with the incompatible modes, $\boldsymbol{\alpha}$, to be zero (Wilson 2002). That is, for a state of constant stress

$$W_I = \frac{1}{2}\int \boldsymbol{\sigma}^T \mathbf{B}_I \boldsymbol{\alpha} dV = 0 \Rightarrow \int \mathbf{B}_I dV = 0 \tag{8}$$

where $\boldsymbol{\sigma} = \{\sigma_x \ \ \sigma_y \ \ \sigma_z \ \ \sigma_{xy} \ \ \sigma_{yz} \ \ \sigma_{zx}\}$ is the stress vector.

This can be satisfied by adding a constant correction matrix, $\mathbf{B}_{IC}$, to the $\mathbf{B}_I$ to form a corrected strain-displacement relationship matrix, $\overline{\mathbf{B}}_I$

$$\overline{\mathbf{B}}_I = \mathbf{B}_I + \mathbf{B}_{IC} \tag{9}$$

The correction matrix can be interpreted as that the work done by the incompatible displacement on the element boundary should vanish when a constant stress field is considered (Wu *et al.* 2001). It is evaluated every time before forming element stiffness matrix. Taking into account that $\mathbf{B}_{IC}$ is a constant matrix, it can be derived that

$$\int (\mathbf{B}_I + \mathbf{B}_{IC}) dV = 0 \Rightarrow \mathbf{B}_{IC} = -\frac{1}{V}\int \mathbf{B}_I dV \tag{10}$$

2.3 Element stiffness matrix

The complete set of element equilibrium equations are given by

$$\begin{Bmatrix} d\mathbf{f} \\ \mathbf{0} \end{Bmatrix} = \begin{bmatrix} \int \mathbf{B}_C^T \mathbf{D} \mathbf{B}_C dV & \int \mathbf{B}_C^T \mathbf{D} \overline{\mathbf{B}}_I dV \\ \int \overline{\mathbf{B}}_I^T \mathbf{D} \mathbf{B}_C dV & \int \overline{\mathbf{B}}_I^T \mathbf{D} \overline{\mathbf{B}}_I dV \end{bmatrix} \begin{Bmatrix} d\mathbf{u} \\ d\boldsymbol{\alpha} \end{Bmatrix} = \begin{bmatrix} \mathbf{K}_{CC} & \mathbf{K}_{CI} \\ \mathbf{K}_{IC} & \mathbf{K}_{II} \end{bmatrix} \begin{Bmatrix} d\mathbf{u} \\ d\boldsymbol{\alpha} \end{Bmatrix} \tag{11}$$

where $\mathbf{D}$ is the constitutive matrix and $d\mathbf{f}$, $d\mathbf{u}$ and $d\boldsymbol{\alpha}$ are the incremental force, nodal displacement and extra DoF vectors, respectively. In elasto-plastic state, the $\mathbf{D}$ should be replaced by $\mathbf{D}^{ep}$ given in Section 3.

The extra DoF, $d\alpha$, can be statically condensed out, so the element stiffness matrix has the same size as the matrix without incompatible enhancement. Finally, the element stiffness matrix with incompatible modes, **K**, is

$$(\mathbf{K}_{CC} - \mathbf{K}_{CI}\mathbf{K}_{II}^{-1}\mathbf{K}_{IC})d\mathbf{u} = d\mathbf{f} \Rightarrow \mathbf{K} = \mathbf{K}_{CC} - \mathbf{K}_{CI}\mathbf{K}_{II}^{-1}\mathbf{K}_{IC} \tag{12}$$

2.4 Incremental strains and internal nodal forces

From Eq. (11), the incremental extra DoF can be expressed as

$$d\alpha = -\mathbf{K}_{II}^{-1}\mathbf{K}_{IC}d\mathbf{u} \tag{13}$$

Accordingly, the incremental Green-Lagrange strains are

$$d\varepsilon = (\mathbf{B}_C d\mathbf{u} + \mathbf{B}_I d\alpha) - d\varepsilon_0 = (\mathbf{B}_C - \mathbf{B}_I\mathbf{K}_{II}^{-1}\mathbf{K}_{IC})d\mathbf{u} - d\varepsilon_0 \tag{14}$$

This incremental strain will be used for calculating the internal nodal forces, $\mathbf{F}_{int}$. It is assumed that the displacement can be large, but the strain is small. In the minimization of the potential energy the forces associated with the incompatible displacement modes are zero (Wilson 2002), therefore

$$\mathbf{F}_{int} = \int \mathbf{B}_C^T \boldsymbol{\sigma} dV \tag{15}$$

where $\boldsymbol{\sigma}$ is the Cauchy stress vector calculated according to the constitutive algorithm given below.

3. Constitutive algorithm at elevated temperatures

3.1 The unified 3D elasto-plastic constitutive relationship

When the deformation is large, material properties tend to be non-linear. Therefore, an incremental stress-strain constitutive relationship should be used, especially when the plastic flow may occur. A general approach is to use the flow rule, which assumes

$$d\varepsilon = d\varepsilon^e + d\varepsilon^p \quad \text{and} \tag{16}$$

$$d\varepsilon^p = \lambda \frac{\partial Q}{\partial \boldsymbol{\sigma}} \tag{17}$$

where Q is the plastic potential, and the superscripts e and p denote elastic and plastic, respectively. λ is the plastic multiplier. In this study, the flow rule is assumed to be associated (i.e., the plastic potential is taken the same as the yield function) and only isotropic hardening is considered. Perfect plastic flow can be treated as a special instance of isotropic hardening which has a zero hardening parameter, H. Thus, the yield function is

$$F(\boldsymbol{\sigma}, w^p) = 0 \tag{18}$$

where w^p is a scalar denoting the plastic work done. Noting that the stress increment is produced by the elastic strain increment only and the plastic work increment is the work done by the stress through plastic strain increment, we have

$$d\boldsymbol{\sigma} = \mathbf{D}d(\boldsymbol{\varepsilon}-\boldsymbol{\varepsilon}^p) = \mathbf{D}\left(d\boldsymbol{\varepsilon}-\lambda\frac{\partial F}{\partial\boldsymbol{\sigma}}\right) \tag{19}$$

and

$$dw^p = \boldsymbol{\sigma}^T d\boldsymbol{\varepsilon}^p = \lambda\boldsymbol{\sigma}^T\frac{\partial F}{\partial\boldsymbol{\sigma}} \tag{20}$$

where $\mathbf{D}$ is the elastic constitutive matrix.

Substituting Eqs. (19) and (20) into the differentiation of Eq. (18), then

$$\left(\frac{\partial F}{\partial\boldsymbol{\sigma}}\right)^T\mathbf{D}\left(d\boldsymbol{\varepsilon}-\lambda\frac{\partial F}{\partial\boldsymbol{\sigma}}\right)+\lambda\frac{\partial F}{\partial w^p}\boldsymbol{\sigma}^T\frac{\partial F}{\partial\boldsymbol{\sigma}} = 0 \Rightarrow \lambda = \frac{1}{a}\left(\frac{\partial F}{\partial\boldsymbol{\sigma}}\right)^T\mathbf{D}d\boldsymbol{\varepsilon} \tag{21}$$

where

$$a = \left(\frac{\partial F}{\partial\boldsymbol{\sigma}}\right)^T\mathbf{D}\frac{\partial F}{\partial\boldsymbol{\sigma}}-\frac{\partial F}{\partial w^p}\boldsymbol{\sigma}^T\frac{\partial F}{\partial\boldsymbol{\sigma}} \tag{22}$$

For isotropic hardening material with von-Mises yield criterion, it can be derived (Bhatti 2006) that $a = 3G+H$, where G is the shear modulus. Finally, substituting Eq. (21) into Eq. (19), the plastic constitutive relationship can be obtained as

$$d\boldsymbol{\sigma} = \mathbf{D}d(\boldsymbol{\varepsilon}-\boldsymbol{\varepsilon}^p) = \mathbf{D}\left(d\boldsymbol{\varepsilon}-\frac{1}{a}\frac{\partial F}{\partial\boldsymbol{\sigma}}\left(\frac{\partial F}{\partial\boldsymbol{\sigma}}\right)^T\mathbf{D}d\boldsymbol{\varepsilon}\right) = \mathbf{D}^{ep}d\boldsymbol{\varepsilon} \tag{23}$$

where the elasto-plastic constitutive matrix, $\mathbf{D}^{ep}$ is

$$\mathbf{D}^{ep} = \mathbf{D}-\underbrace{\frac{1}{a}\mathbf{D}\frac{\partial F}{\partial\boldsymbol{\sigma}}\left(\frac{\partial F}{\partial\boldsymbol{\sigma}}\right)^T\mathbf{D}}_{\mathbf{D}^p} = \mathbf{D}-\mathbf{D}^p \tag{24}$$

A unified form of $\partial F/\partial\boldsymbol{\sigma}$ has been given in (Owen and Hinton 1980) as

$$\frac{\partial F}{\partial\boldsymbol{\sigma}} = C_1\mathbf{a}_1+C_2\mathbf{a}_2+C_3\mathbf{a}_3 \tag{25}$$

where C_1, C_2, C_3, $\mathbf{a}_1$, $\mathbf{a}_2$ and $\mathbf{a}_3$ can be found in Appendix (Owen and Hinton 1980).

3.2 State determination procedure at ambient temperature

In nonlinear analysis, the element stiffness and the nodal internal forces change with material state at the Gaussian integration points. At ambient temperature, the state determination procedure is summarized as (Owen and Hinton 1980, Bhatti 2006):

(1) Calculate the trial stress increment: $\boldsymbol{\sigma} = \boldsymbol{\sigma}_0+\Delta\boldsymbol{\sigma} = \boldsymbol{\sigma}_0+\mathbf{D}\Delta\boldsymbol{\varepsilon}$.

(2) Compute the yield function $F\boldsymbol{\sigma})$. If $F < 0$, then the trial stress is OK, the material stays elastic for previously elastic state or unloads elastically for previously plastic state. Although unloading

may eventually ends outside of the yield function (Bhatti 2006), in static incremental analysis, this rarely happens. Otherwise, further treatment is required as follows.

(3) If the previous state is elastic, then calculate the proportion of the stress outside of the yield surface, R. The trial stress is then adjusted by $-R\Delta\boldsymbol{\sigma}$. The state changes to plastic. The remaining incremental strain $R\Delta\boldsymbol{\varepsilon}$ is related to plastic flow moving along the yield surface. If the previous state is plastic then $R = 1$.

(4) To avoid the stress calculated drifting away too much from the yield surface, forward Euler integration method can be used. This is done by subdividing the $R\Delta\boldsymbol{\sigma}$ into a number of sub-steps, then increase the incremental plastic strains step by step. A suggested number of steps (Owen and Hinton 1980) is

$$n = 8\left(\frac{\sigma_{eff} - \sigma_y}{\sigma_y^0}\right) + 1 \tag{26}$$

where σ_{eff}, σ_y and σ_y^0 are the effective, yield and initial yield stresses, respectively. This explicit method has no error control; however, it is the simplest and an effective way.

It is clear that the stress-strain relationship is influenced by its past history according to the state determination procedure provided above. During a Newton-Raphson iteration, an element may inaccurately enter plastic state and causes underestimated stresses for internal force calculation and accumulated plastic strain. This is a potential source of inaccuracy. A simple way to avoid this problem (Bhatti 2006) is to use the accumulated displacement from the beginning of the current load step instead of the increment from the current iteration. Only after the solution has converged then the element state can be updated. But the new tangent stiffness matrix must use the current state of the element.

3.3 Moving beyond the initially converged stress locking at elevated temperatures

A general procedure in structural fire engineering analysis is to apply all the mechanical loads at ambient temperature, then increase the temperature step by step:

(1) Performing thermal analysis to obtain the history of temperature distribution in the structure at specified time intervals.

(2) Carrying out structural analysis at ambient temperature by applying the total mechanical loads in a number of steps.

(3) With the loads kept constant, updating the elemental temperatures step by step using the temperature data obtained in (1).

(4) The structural analysis continues until the structure run away (numerical failure) or the end of the fire scenario.

Materials exhibit mechanical property degradation and thermal expansion at elevated temperatures. Figs. 2(a) and (b) show this transformation of the Young's modulus, E, and the yield strength, σ_y given in Eurocode 3 (BS EN 1993-1-2 2005), in which the effects of transient thermal creep have been included implicitly. Therefore, the yield surface shrinks (Fig. 3) with increase of temperature, which triggers an alternative loading event should the stress go beyond this surface boundary. On the contrary, cooling leads to the expansion of yield surface and consequently triggers unloading from yield state to elastic state.

The material state determination procedure stated in Section 3.2 works fine at ambient

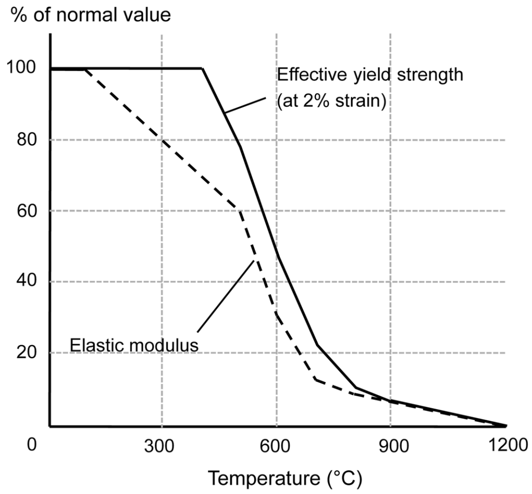

(a)

Fig. 2(a) Mechanical property degradation of structural steel at elevated temperatures (BS EN 1993-1-2 2005)

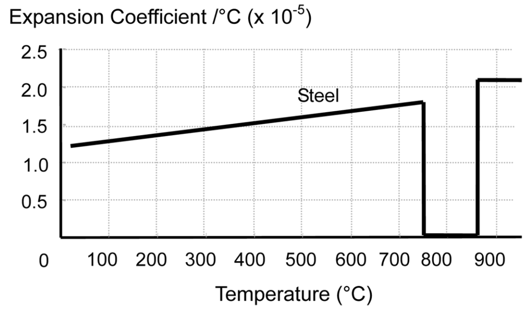

(b)

Fig. 2(b) Thermal expansion of structural steel at elevated temperatures (BS EN 1993-1-2 2005)

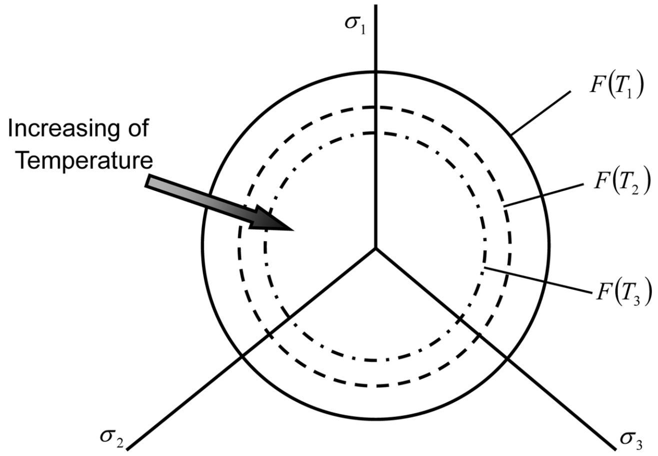

Fig. 3 Von-Mises yield surface, F(T), of steel subject to elevated temperatures

temperature. However, while the external load is kept constant in the stage of elevating temperature, it is found that the material degradation has no influence on the increasing displacements. This can be illustrated as follows:

Supposing $\boldsymbol{\sigma}_0$ is the stress attained at step n and is used as the initially converged stress in step $n+1$. In step $n+1$ the external load is kept constant and undergoes a temperature increment, ΔT. Material property degradation leads to an incremental displacement $\Delta\mathbf{d}$ in the first iteration of step $n+1$. Subsequently, an incremental strain $\Delta\boldsymbol{\varepsilon}$ can be calculated and used in the material state determination. That is, $\boldsymbol{\sigma}_0 + \mathbf{D}\Delta\boldsymbol{\varepsilon}$ is used as the trial stress (see (1) in Section 3.2). Supposing the material state stays linear elastic, this trial stress is regarded as the new stress and used to evaluate

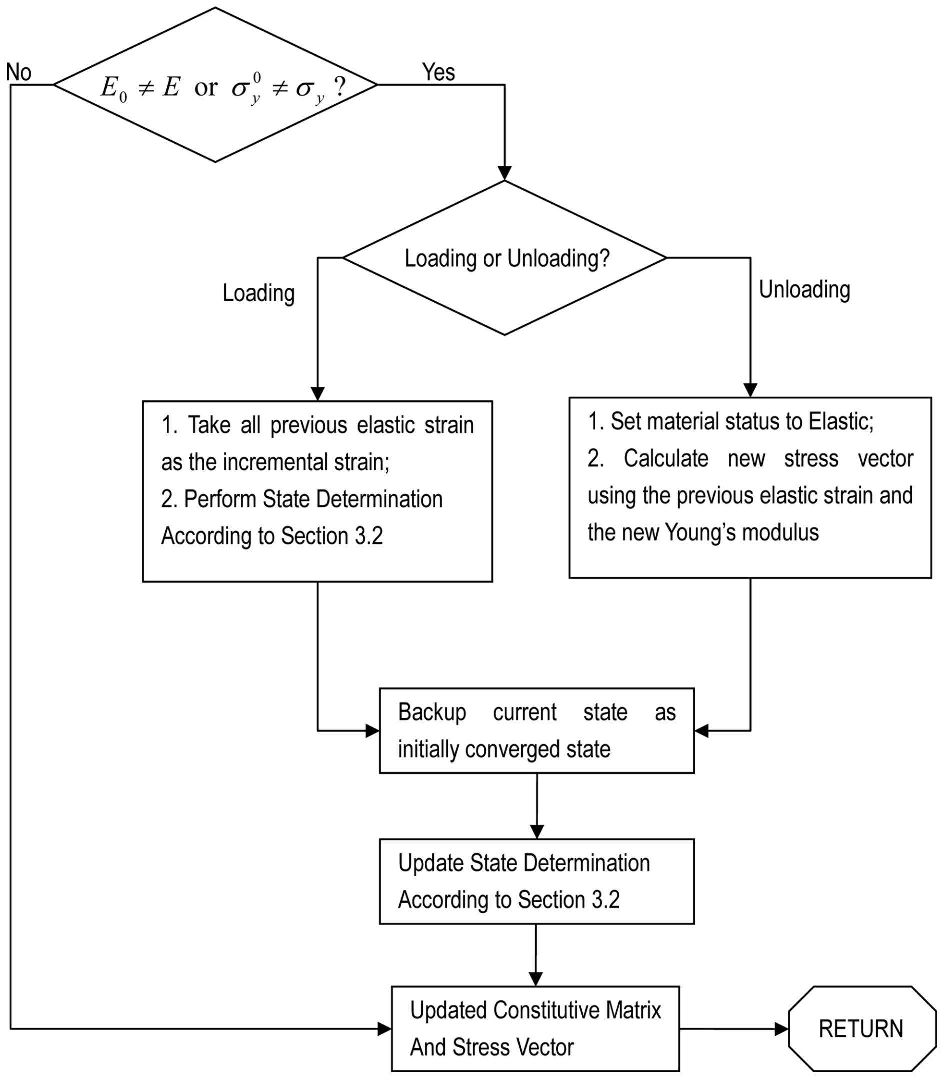

Fig. 4 Flow chart of material state determination at elevated temperatures

the internal nodal force which is definitely unequal to the external load applied. Then a counteracting displacement increment is required in the subsequent iterations to balance the internal and external forces. Finally, the displacement seems as if being locked although material degradation undergoes. An example of locking is given in Section 4.2.1.

As this locking phenomenon has never been reported before, a simple solution is developed to break this locking by re-determinating and updating the material state at the beginning of each step of temperature increment, with all the elastic strain taken as the incremental strain. Assuming Young's modulus E and yield stress σ_y are positively associated then the algorithm chart can be drawn as shown in Fig. 4. This can be used as a supplement to the step (4) in the general structural fire analysis procedure illustrated above.

4. Numerical studies

Several numerical studies carried out in this research are based on a structural steel cantilever beam as shown in Fig. 5. If not specified, the Young's modulus is assumed to be 2×10^5 MPa and the Poisson's ratio is assumed to be 0.3.

4.1 Computational efficiency of SOLID8IC

In order to show the effectiveness of eliminating shear locking, numerical studies on the steel cantilever beam (Fig. 5) are analyzed using compatible (*SOLID8C*) and the current incompatible models. It is hereby assumed that the material is perfectly linear, and the end point load P is 1600 N applied gradually in 20 steps. The cross section dimension is $b = d = 20$ mm, the length L is 1000 mm. The cantilever beam is equally discretized into 25, 50 and 500 elements. The comparison of the end point displacements and the maximum shear stresses at the Gaussian integration point in the element next to support are shown in Table 1. It is obvious from the table that *SOLID8IC* can effectively eliminate the parasitic shear stresses in *SOLID8C* elements. The end displacements and maximum shear stresses modelled by the *SOLID8IC* with various numbers of elements are stable. Although accurate results can be achieved by very fine mesh of compatible elements, the inefficiency is apparent. The geometric nonlinear behaviour can be seen from the end displacement of the cantilever modelled by 25 *SOLID8IC* elements shown in Fig. 6.

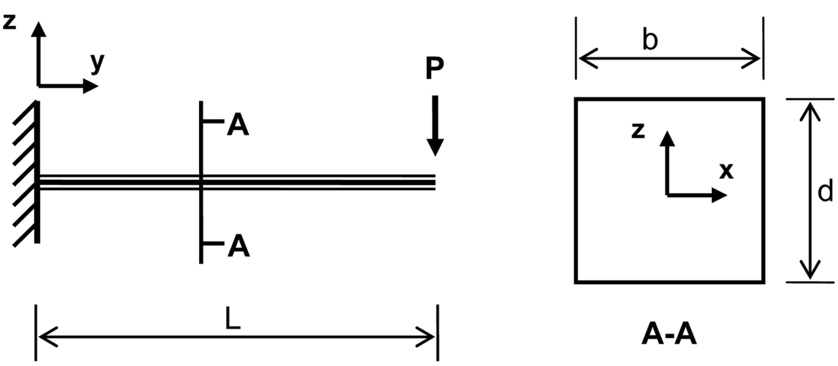

Fig. 5 Steel cantilever beam subjected to concentrated load, P

Table 1 Comparison the performance of the *SOLID8IC* and *SOLID8C*

Discretization	End Point Displacement (mm)		Maximum τ_{yz} (MPa)	
	SOLID8IC	SOLID8C	SOLID8IC	SOLID8C
25E	191.7175	72.9512	5.6406	209.0871
50E	192.1281	132.9855	4.8399	193.1995
500E	192.3795	181.5735	4.0696	30.5179
Exact	192.0*			

*Timoshenko beam solution (Gere and Timoshenko 1990)

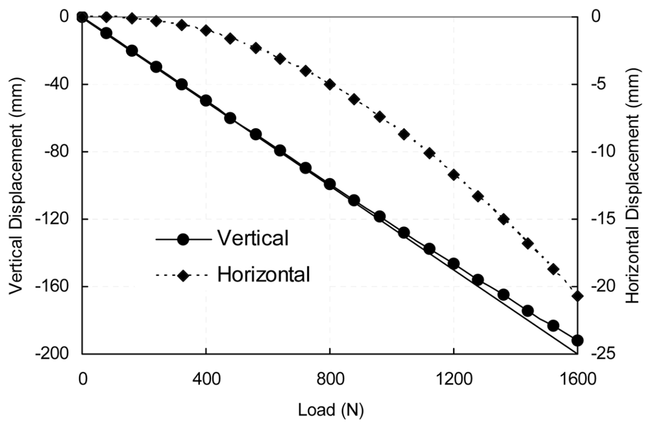

Fig. 6 The end displacement of the cantilever modelled by 25 *SOLID8IC* elements

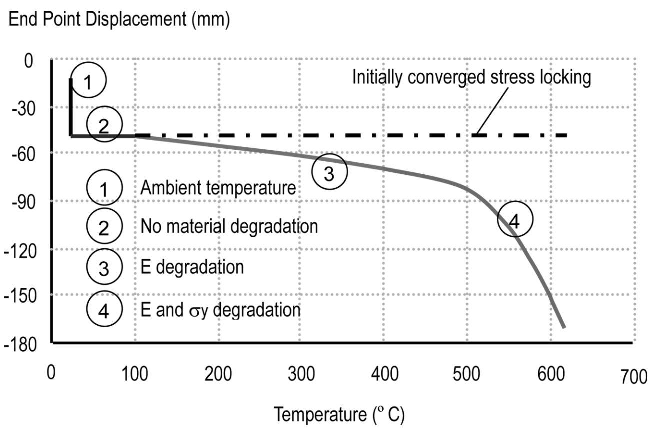

Fig. 7 Mechanisms of thermally induced effects on the behaviour of a steel cantilever beam

4.2 Thermally induced effects in structural analysis

The steel properties at elevated temperatures given in Figs. 2(a) and (b) are adopted in this study. The degradation of the E starts from 100ºC and the σ_y starts from 400ºC.

4.2.1 Mechanisms due to thermally induced material nonlinearity

Analysis is conducted on the steel cantilever beam used previously in Section 4.1 but the vertical point load is reduced to 400 N. This load is applied at ambient temperature and then kept constant when the temperature is raised step by step at 20ºC intervals. The relationship between the temperature and the vertical tip displacement modelled is shown in Fig. 7. The result shows a trivial vertical displacement reduction when the temperature is increased to 100ºC. This is because there is almost no material degradation before 100ºC. After the temperature of the beam exceeds 100ºC, the Young's modulus, E, starts to degrade. The degradation of the yield strength initiates when temperature reaches 400ºC. It is also shown in this figure that the initially converged stress locking suppresses the beam from further deformation at elevated temperatures.

4.2.2 Thermally induced stresses due to non-uniform cross-sectional temperature distribution

A numerical study on gradient temperature distribution in the cross section is carried out on a steel cantilever beam. The schema in Section 4.1 is reused, except the depth of the cross-section of the beam (d), which is reduced to 10 mm. No external load is applied. The beam is equally discretized into 5 elements in the depth direction of the cross-section and 50 elements in the longitudinal direction. Linear temperature distribution from the bottom to top is assumed. The bottom layer element temperature is increased by 20ºC in each step. Whereas the top layer element temperature is kept as 20ºC. The main purpose of this assumption is to generate a very extreme temperature gradient case in order to see the impact of thermal stress on the structural behaviour of the beam. The yield stress at ambient temperature is assumed to be 460 MPa. In order to compare with the beam-column line element model, the beam cross section is allowed to expand freely avoiding thermal expansion induced lateral constrain at the fixed support. Apparently, the beam is to bow upwards due to non-uniform thermal expansion. At the same time, the material strength and stiffness degrade with increase of temperature. The comparison of the end-displacements predicted by current element and the fibre-section beam element in structural fire engineering software Vulcan (Huang *et al.* 2009) developed at the University of Sheffield is given in Fig. 8. It can be seen that the results agree very well with each other. The stresses at the Gaussian integration points in the fix-end bottom element are plotted in Fig. 9. However, this stress pattern cannot be modelled by beam elements.

In Fig. 9, the normal stresses of *sx, sy* and *sz* are referenced to global coordinate, *x, y, z,* respectively (see Fig. 5). It is clear that *sx, sy* exhibit increasing in tension then gradually descending at high temperature. This is because of the thermal expansion mismatch between the elements. According to the Eurocode 3, the thermal expansion coefficient (see Fig. 2(b)) of steel increases from less than 1.0×10^{-5}/C at 20C to more than 4.2×10^{-5}/C at 700ºC. The expansion suspends between 750ºC and 860ºC due to crystal phase transformation. When the temperature is not too high, the expansion in the bottom layer elements is not big enough to match that in mid-layer elements (i.e., the bottom layer has a longer lever arm to the neutral axis). Further heating

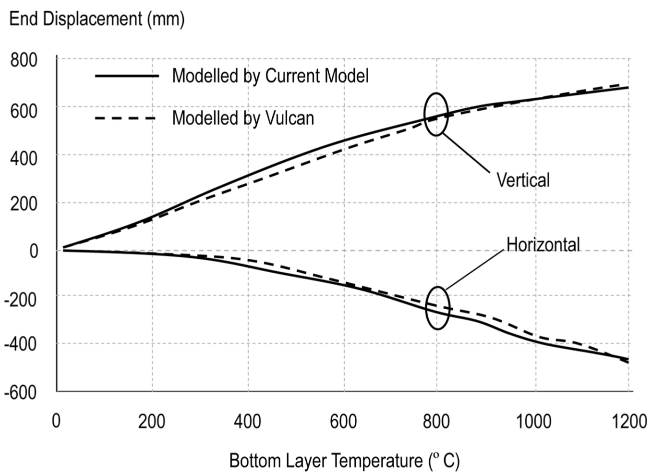

Fig. 8 Comparison of the end displacements of a cantilever beam subjected to gradient temperature, modelled by current model and the Vulcan (Huang *et al.* 2009) beam model

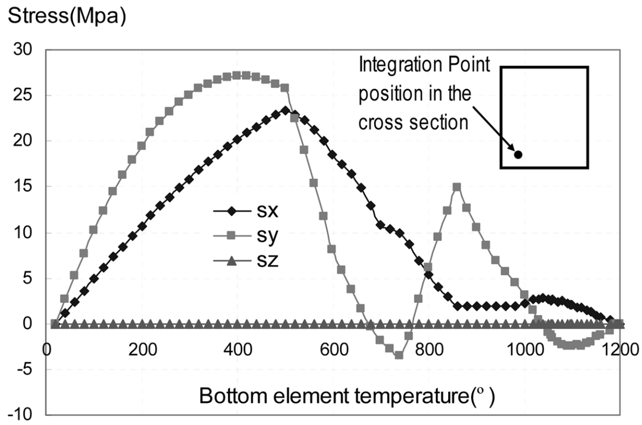

Fig. 9 Stresses at the Gaussian integration point in the element adjacent to the fix-end free of lateral expansion (*sx*, *sy* and *sz* are stresses in the *x*, *y* and *z* directions, see Fig. 5)

gradually reduces this difference, and the Young's modulus at the bottom layer elements degrades faster than that in mid-layer elements. In the phase of transformation, thermal expansion stops, which can be reflected by the second ascending in the curve of *sy* in Fig. 9. Nevertheless, the magnitude of the stresses is small.

4.2.3 Modelling of simply supported beam with gradient longitudinal temperature

A beam fire test (Chen *et al.* 2005) was carried out at State Key Laboratory of Fire Science, USTC, China. The simply supported specimen was a thin-wall hollow section beam fabricated by Q215 steel ($f_y \geq 215$ MPa, $f_u = 315 - 410$ MPa). Two point loads were applied as shown in Fig. 10. The beam was non-uniformly heated so that the left of the beam was hotter than the right. Five equally distributed thermal gauges (TS1-TS5 in Fig. 10) were used to measure the surface temperature distribution along the beam. Because the wall thickness of the beam is only 2 mm, the surface temperatures measured (see Fig. 11) are used as longitudinal sampling temperatures of the beam for numerical modelling. The temperature distribution in the cross section is assumed to be uniform. It can be seen from Fig. 11 that the maximum temperature difference between both ends of

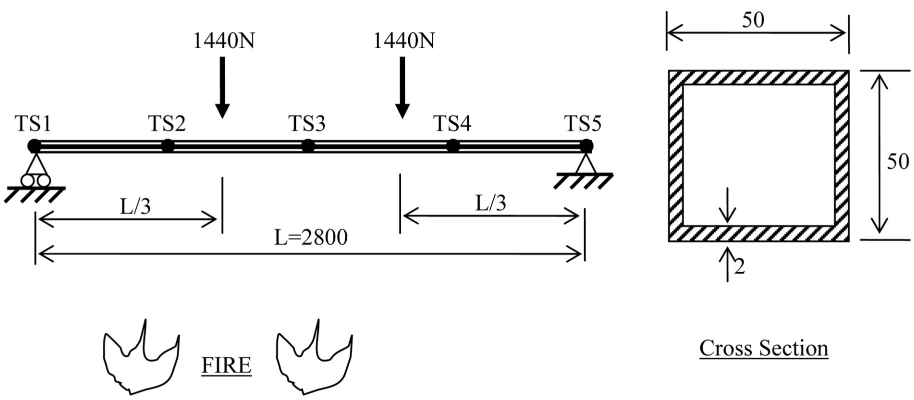

Fig. 10 Plan of the USTC hollow section steel beam subjected to non-uniform heating

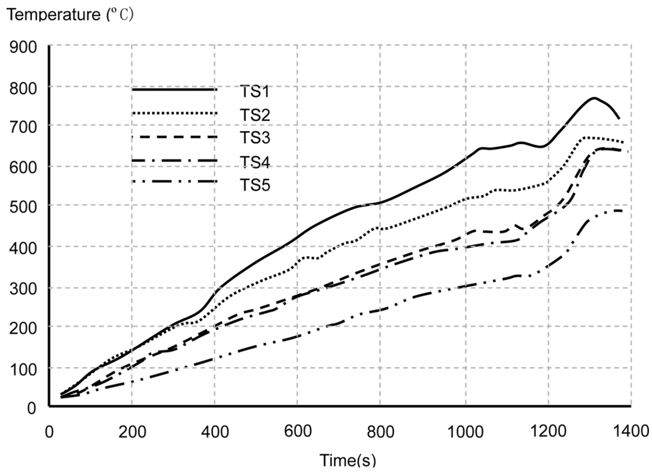

Fig. 11 Surface temperature distribution along the USTC beam in fire test

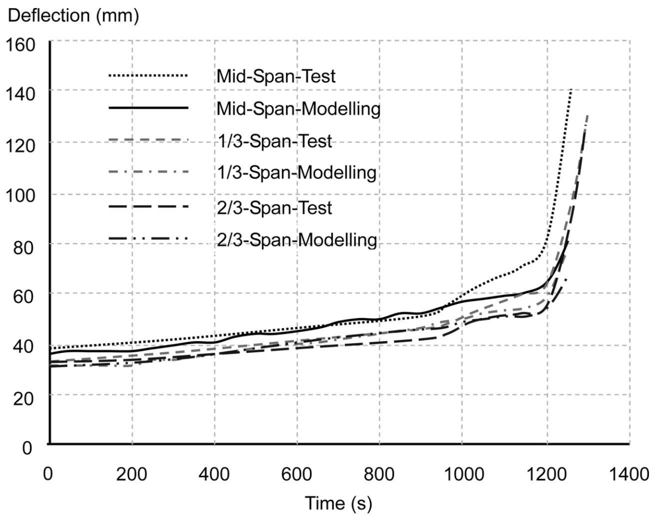

Fig. 12 Comparison of predicted and measured displacements at different positions of the USTC beam in fire

the beam exceeds 300°C. The specimen is divided into 1800 *SOLID8IC* elements with temperatures linearly interpolated from the temperatures at the sampling positions. The Young's modulus and Poisson's ratio are assumed to be 206000 MPa and 0.3, respectively. Other material properties are assumed to follow those given in Eurocode 3. The comparison of the results measured and predicted is shown in Fig. 12. The temperature on the left is higher than that on the right, consequently, the deflection is larger at 1/3 span than at 2/3 span counting from the left hand support of the beam. It can be seen from Fig. 12 that the deflections modelled agree very well with test results before 1000 seconds of fire. The discrepancy increases later on. This might come from the temperature distribution and the material properties used in the modelling. Another reason may stem from the viscous creep when the temperatures approaching to critical ones. The stress-strain relationships at 1/3 span and mid-span are shown in Fig. 13. It can be seen that at elevated temperatures, the stress has very little increase while the strain increases due to softening and

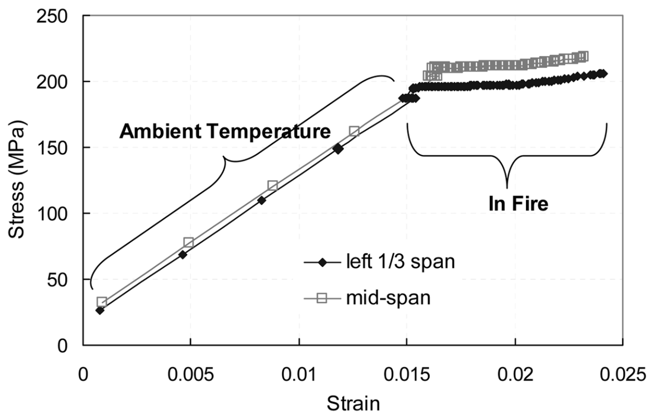

Fig. 13 The stress-strain relationships modelled at 1/3 span and mid-span

increased ductility in fire as illustrated previously (see Fig. 2(a)).

5. Conclusions

An 8-node 3D solid element enhanced with incompatible bending mode incorporated with a unified 3D constitutive model is developed for modelling structural members subject to bending at elevated temperatures. However, it is found that the traditional incremental material state determination algorithm can not handle material degradation properly due to initial converged stress locking at elevated temperatures. Therefore, an algorithm is proposed to overcome this problem. A cantilever beam with various temperature distribution schemes and a simply supported beam with a non-uniform longitudinal temperature distribution are modelled. It is shown from these numerical studies that this *SOLID8IC* element can effectively eliminate shear locking. And the comparison of the numerical results with other structural fire engineering software modelling and experiment data shows that the model and algorithm developed in this study are robust and can be used for 3D structural analysis of steel members at elevated temperatures.

Acknowledgements

The authors would like to gratefully acknowledge the valuable comments and suggestions from the reviewers in improving the quality of this paper.

References

Abed-Meraim, F. and Combescure, A. (2011), "New prismatic solid-shell element: assumed strain formulation and hourglass mode analysis", *Struct. Eng. Mech.*, **37**(2), 253-256.

Bathe, K.J. (1996), *Finite Element Procedure*, Prentice Hall.

Bhatti, M.A. (2006), *Advanced Topics in Finite Element Analysis of Structures with Mathematica and Matlab*

Computations, John Wiley & Sons.
BS EN 1993-1-2:2005: Eurocode 3: *Design of Steel Structures*, Part 1-2: "General rules--Structural fire design".
Chen, C., Yao, B., Yang, Y., Cai, X., Zhang, H. and Wan, Y. (2005), "Experimental study on temperature distribution and response behaviors of steel element under corner fire conditions", *Eng. Sci.*, **7**(9), 70-75.
Cook, R.D., Malkus, D.S., Plesha, M.E. and Witt, R.J. (2002), *Concepts and Applications of Finite Element Analysis*, 4th edition, John Wiley & Sons.
Dominguez, N., Fernandez, M.A. and Ibrahimbegovic, A. (2010), "Enhanced solid element for modelling of reinforced concrete structures with bond-slip", *Comput. Concrete*, **7**(4), 347-364.
Gere, J.M. and Timoshenko, S.P. (1990), *Mechanics of Materials*, 3rd edition, PWS-KENT Publishing Company, Boston.
Huang, Z., Burgess, I.W. and Plank, R.J. (2009), "Three-dimensional analysis of reinforced concrete beam-column structures in fire", *J. Struct. Eng.-ASCE*, **135**(10), 1201-1212.
Hughes, T.J.R. (1980), "Generalization of selective integration procedures to anisotropic and nonlinear media", *Int. J. Numer. Meth. Eng.*, **15**, 1413-1418.
Ibrahimbegovic, A. and Wilson, E.L. (1991), "A modified method of incompatible mode"s, *Comm. Appl. Numer. Meth.,* **7**(3), 187-194.
Irons, B.M. and Razzaque, A. (1972), *Experience with the Patch Test for Convergence of finite Element Method*, Mathematical Foundations of the Finite Element Methods, Academic Press, New York.
Owen, D.R.J. and Hinton, E. (1980), *Finite Elements in Plasticity: Theory and Practice*, Pineridge Press.
Simo, J.C. and Rafai, M.S. (1974), "A class of assumed strain method and incompatible modes", *J. Numer. Meth. Eng.*, **29**(8), 1595-1638.
Taylor, R.L., Simo, J.C., Zienkiewicz, O.C. and Chan, A.H.C. (1986), "The patch test – a condition for assessing FEM convergence", *Int. J. Numer. Meth. Eng.*, **22**, 39-62.
Wilson, E.L., Taylor, R.L., Doherty, W.P. and Ghaboussi, J. (1971), "In compatible displacement models", *Symposium on Numerical and Computer Method in Structural Mechanics*, University of Illinois, Urbana.
Wilson, E.L. (2002), *Three-Dimensional Static and Dynamic Analysis of Structures - A Physical Approach with Emphasis on Earthquake Engineering*, 3rd edition, Computers and Structures Inc.
Wu, C.C., Huang, Y.Q. and Ramm, E. (2001), "A further study on incompatible models: revise-stiffness approach and completeness of trial functions", *Comput. Meth. Appl. Mech. Eng.*, **190**, 5923-5934.

Appendix

Constants defining the unified yield surface for numerical analysis (Owen and Hinton 1980)

$$\mathbf{a}_1 = \{1 \quad 1 \quad 1 \quad 0 \quad 0 \quad 0\}^T$$

$$\mathbf{a}_2 = \frac{1}{2\sqrt{J_2}}\{\sigma_x^d \quad \sigma_y^d \quad \sigma_z^d \quad 2\tau_{yz} \quad 2\tau_{zx} \quad 2\tau_{xy}\}^T$$

$$\mathbf{a}_3 = \{\sigma_y^d\sigma_z^d - \tau_{yz}^2 + \frac{J_2}{3}, \quad \sigma_x^d\sigma_z^d - \tau_{xz}^2 + \frac{J_2}{3}, \quad \sigma_x^d\sigma_y^d - \tau_{xy}^2 + \frac{J_2}{3},$$
$$2(\tau_{xz}\tau_{xy} - \sigma_x^d\tau_{yz}), \quad 2(\tau_{xy}\tau_{yz} - \sigma_y^d\tau_{xz}), \quad 2(\tau_{yz}\tau_{zx} - \sigma_z^d\tau_{xy})\}^T$$

Yield Criterion	C1	C2	C3
Tresca	0	$2\cos\theta(1+\tan\theta\tan 3\theta)$	$\frac{\sqrt{3}}{J_2}\frac{\sin\theta}{\cos 3\theta}$
Von Mises	0	$\sqrt{3}$	0
Coulomb-Mohr	$\frac{1}{3}\sin\phi$	$\cos\theta[(1+\tan\theta\tan 3\theta) + \sin\phi(\tan 3\theta - \tan\theta)/\sqrt{3}]$	$\frac{\sqrt{3}\sin\theta + \cos\theta\sin\phi}{2J_2\cos 3\theta}$
Drucker-Prager	α	1.0	0

Note: ϕ is the internal friction angle of material, e.g., concrete
θ is the similarity angle
J_2 is the second deviatoric stress invariant
σ_x^d, σ_y^d and σ_z^d are axial deviatoric stresses

$$\alpha = \frac{2\sin\phi}{\sqrt{3}(3-\sin\phi)}$$